JOURNAL OF PROPULSION AND POWER
Vol. 16, No. 6, November–December 2000

Computational Analysis for Rocket-Based Combined-Cycle Systems During Rocket-Only Operation

C. J. Steffen, Jr.,* T. D. Smith,† and S. Yungster‡
NASA John H. Glenn Research Center, Cleveland, Ohio 44135
and
D. J. Keller§
Real World Quality Systems, Inc., Rocky River, Ohio

A series of Reynolds-averaged Navier–Stokes calculations were employed to study the performance of rocket-based combined-cycle systems operating in an all-rocket mode. This parametric series of calculations were executed within a statistical framework, commonly known as design of experiments. The parametric design space included four geometric and two flowfield variables set at three levels each, for a total of 729 possible combinations. A D-optimal design strategy was selected. It required that only 36 separate computational fluid dynamics (CFD) solutions be performed to develop a full response surface model, which quantified the linear, bilinear, and curvilinear effects of the six experimental variables. The axisymmetric, Reynolds-averaged Navier–Stokes simulations were executed with the NPARC v3.0 code. The response used in the statistical analysis was created from I_{sp} efficiency data integrated from the 36 CFD simulations. The influence of turbulence modeling was analyzed by using both one- and two-equation models. Careful attention was also given to quantify the influence of mesh dependence, iterative convergence, and artificial viscosity upon the resulting statistical model. Thirteen statistically significant effects were observed to have an influence on rocket-based combined-cycle nozzle performance. It was apparent that the free-expansion process, directly downstream of the rocket nozzle, can influence the I_{sp} efficiency. Numerical schlieren images and particle traces have been used to further understand the physical phenomena behind several of the statistically significant results.

Nomenclature

A	=	area
A_r/A^*	=	primary rocket nozzle area ratio (see Fig. 1)
A_3/A^*	=	mixer-ejector inlet area ratio (see Fig. 1)
A_6/A_3	=	mixer-ejector exit area ratio (see Fig. 1)
c_i	=	constant coefficient of statistical model
D	=	diameter
I_{sp}	=	vacuum specific impulse
L	=	mixer-ejector nozzle length (see Fig. 1)
L/D_3	=	mixer-ejector length/diameter ratio (see Fig. 1)
l_{ref}	=	reference length
$\dot{m}$	=	propellant mass flow
$\dot{m}_s/\dot{m}_p$	=	secondary mass-flow injection ratio
P_c	=	rocket chamber total pressure
p	=	static pressure
Re_{ref}	=	Reynolds number at throat conditions
T_0	=	rocket chamber total temperature
$\bar{T}$	=	axial thrust
u	=	velocity
x_i	=	independent variable of statistical model (see Table 1)
$\hat{x}_i$	=	transformed independent variable [see Eq. (1)]
α	=	grid refinement ratio
β	=	spatial order of accuracy of computational fluid dynamics solution
$\eta_{I_{sp}}$	=	vacuum specific impulse efficiency
ρ	=	density

Subscripts

cav	=	annular cavity
p	=	primary
r	=	rocket nozzle
s	=	secondary
3	=	mixer-ejector inlet
6	=	mixer-ejector exit

Superscripts

CFD	=	calculated from the computational fluid dynamics flow solution
MAX	=	calculated from isentropic flow theory
RSM	=	calculated from response surface model
*	=	rocket throat

Received 29 October 1998; revision received 14 March 2000; accepted for publication 24 March 2000.

*Aerospace Engineer, Turbomachinery and Propulsion Systems Division. Senior Member AIAA.
†Aerospace Engineer, Turbomachinery and Propulsion Systems Division. Senior Member AIAA.
‡Research Associate, Institute for Computational Mechanics in Propulsion. Senior Member AIAA.
§President.

I. Introduction

REUSABLE launch vehicles have many potential economic benefits. Currently, several single-stage-to-orbit propulsion concepts are under investigation within NASA's Advanced Space Transportation program. One of the most promising technologies receiving renewed attention is rocket-based combined-cycle (RBCC) propulsion.

RBCC propulsion systems have been studied for many years. Much of the analysis to date can be traced back to the foundation established three decades ago.[1] Currently, several organizations, academic and industrial, are investigating the possibilities of RBCC propulsion.[2–4] Olds and Lee[5] and Olds[6] have conducted qualitative multidisciplinary design optimization and economic analysis for a variety of RBCC vehicles. Often, such analyses will hinge upon assumed values of engine component efficiencies. However, a truly robust design optimization demands further investigation into the subsystem performance of these complex propulsion cycles.

The RBCC concept considered here is defined by four separate operational modes in a single-stage-to-orbit configuration. First, the engine functions as a rocket-driven ejector (mode 1). Then the rocket engine is switched off, and subsonic combustion is present in the ramjet (mode 2). As the vehicle continues to accelerate, supersonic combustion occurs in the scramjet (mode 3). The rocket is eventually reignited (mode 4) for the final ascent to orbit in an all-rocket mode. The overall performance of the combined-cycle engine is heavily dependent upon the efficiency of this all-rocket mode because a significant portion of the propellant mass is consumed during this final ascent mode. The present study focused upon the engine performance of this fourth and final mode. Engine performance was measured in terms of the thrust generated from a given amount of propellant, or vacuum specific impulse, I_{sp}. This value was compared to the maximum achieved via isentropic expansion to obtain values of I_{sp} efficiency.

Mode 4 can be simulated with the familiar geometry of a ducted rocket. Geometries of this type have been studied extensively for applications concerning rocket driven diffuser flows,[7] base-pressure studies,[8] and supersonic sudden expansions.[9] However, the present study sought to quantify the expansion efficiency of a ducted rocket flow, exhausting to a vacuum, over a wide range of geometric and flow conditions.

We examined the performance of RBCC systems operating in mode 4 with computational fluid dynamics (CFD). The primary reason for choosing numerical simulation over physical experimentation was the inherent cost advantage for a test program of this magnitude and complexity. NPARC v3.0 (Ref. 10) was chosen because of the extensive validation for propulsion flows, including ducted rockets[11,12] and the variety of simulation options.

We chose to execute the CFD simulations within the context of statistical Design of Experiments (DOE).[13] Problem complexity necessitated this approach. The application of DOE methods within the aerospace research community is still relatively new,[14] despite being well established in other fields. Giunta et al.[15] applied a novel DOE method to optimize the configuration of a supersonic transport aircraft using a hierarchy of aerodynamic models. Knill et al.[16] applied response surface methodology (RSM) designs to optimize the configuration of a high-speed civil transport aircraft using Euler flow analysis. Tolle[17] applied RSM and Navier–Stokes flow analysis to optimize the definition of a hypersonic wind-tunnel nozzle contour. We applied RSM designs and Navier–Stokes calculations to analyze RBCC nozzle efficiency over a broad range of parameters.

We varied six independent parameters simultaneously to study their effects upon system performance. A full parametric study of these six variables, each at three levels, would necessitate an enormous computational effort. DOE methods minimize the number of experiments, based upon the anticipated relationships between the response and the independent variables under investigation. This approach yielded a quantitative analysis of a generic RBCC nozzle performing in all-rocket mode. The significant factors influencing this performance have been estimated for future experimental analysis. In addition, the present effort will help the propulsion system designer to focus upon the most important aspects when engaged in a trade study.

II. Nozzle Configuration

A generic RBCC nozzle operating in mode 4 can be represented by three simple components: the primary rocket engine, the annular secondary flow cavity, and the mixer-ejector duct (see Fig. 1). The relevant flow features can be represented by two propellant flowpaths: the primary flow through the rocket thrust chamber and the relatively small secondary flow injected into the annular cavity region. The opportunity for utilizing a secondary mass-flow injection scheme would arise from the specification of a gas-generator engine cycle. For the present study a generic RBCC nozzle configuration was parameterized with the following two flowfield and four geometric variables: rocket chamber total pressure P_c, secondary mass-flow injection ratio $\dot{m}_s/\dot{m}_p$, mixer-ejector inlet area ratio A_3/A^*, mixer-ejector length/diameter ratio L/D_3, mixer-ejector exit area ratio A_6/A_3, and primary rocket nozzle area ratio A_r/A^*. These assumptions led to the parametric design space depicted in Fig. 1 and Table 1. We have intentionally chosen a broad design space for investigation so that the resulting statistical model of nozzle efficiency will encompass a wide range of performance variation. The transformation shown in Eq. (1) was used to scale each independent variable to a $(-1, +1)$ range.

Table 1 Independent variables: definition of the six-dimensional design space

Independent variable	Physical variable	Low	Mid	High
x_1	P_c (psi)	300	750	1200
x_2	$(\dot{m}_s/\dot{m}_p) \times 100\%$	0	4	8
x_3	(A_3/A^*)	40	120	200
x_4	(L/D_3)	2	3.5	5
x_5	(A_6/A_3)	1	1.5	2
x_6	(A_r/A^*)	4	12	20

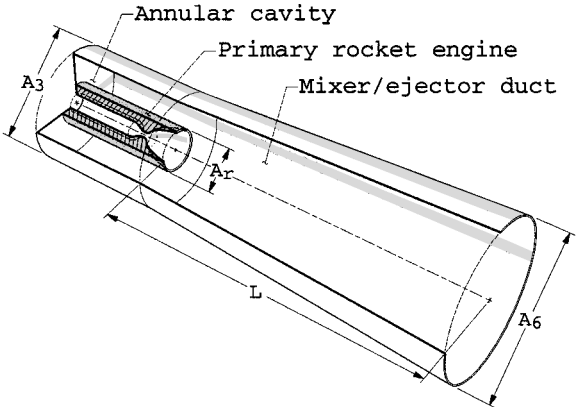

Fig. 1 Axisymmetric RBCC nozzle geometry: A_r denotes the rocket exit area, A_3 denotes the mixer-ejector inlet area, L denotes the mixer-ejector length, A_6 denotes the mixer-ejector exit area, and A^* (not shown) denotes the primary rocket throat area.

$$\hat{x}_i = \frac{2x_i - \left(x_i^{\text{high}} + x_i^{\text{low}}\right)}{\left(x_i^{\text{high}} - x_i^{\text{low}}\right)} \tag{1}$$

Thus $x_i \in [x_i^{\text{low}}, x_i^{\text{mid}}, x_i^{\text{high}}]$, whereas $\hat{x}_i \in [-1, 0, +1]$. This transformation simplified the statistical analyses presented later.

III. Nozzle Efficiency

The integrals for axial mass flow and vacuum thrust were calculated with a trapezoidal integration across the exit of the duct. The ratio of these integrals defined the specific impulse for a given simulation.

$$I_{\text{sp}} = \frac{|\vec{T}|}{\dot{m}_p} = \frac{\int_{A_6}(\rho u^2 + p)\,\mathrm{d}A}{\int_{A_6}(\rho u)\,\mathrm{d}A} \tag{2}$$

$$\eta_{I_{\text{sp}}} = \frac{I_{\text{sp}}^{\text{CFD}}}{I_{\text{sp}}^{\text{MAX}}} \times 100\% \tag{3}$$

Isentropic flow theory defined the maximum specific impulse that a given configuration can achieve. Thus the ratio of the calculated and isentropic impulse values defined the impulse efficiency. The isentropic analysis accounted for the flow through the primary rocket engine alone; any additional injected flow is not reflected in the denominator of the efficiency. An alternate definition and analysis, based upon the gas generator cycle, was presented in Ref. 18.

IV. Numerical Modeling

A. NPARC v3.0

The CFD simulations were performed with version 3 of the NPARC code configured to solve the axisymmetric Navier–Stokes equations. Two different turbulence models were examined so that

Table 2 Combustion chamber specifications for the three total pressure values

Physical variable	Condition 1	Condition 2	Condition 3
P_c psi	300	750	1,200
T_0 °R	6,200	6,400	6,500
Re_{ref}	321,000	323,000	324,000

modeling sensitivity could be addressed. The two turbulence models chosen for examination were the Spalart–Allmaras (SA) one-equation model,[19] and the Chien (k–ε) two-equation model for compressible flows.[20,21]

B. Boundary Conditions

The thrust chamber inflow was specified with constant total pressure, total temperature, and flow angle. The physical walls of this nozzle were modeled with an adiabatic no-slip surface. The exit plane of the mixer-ejector was modeled with an extrapolation boundary condition to simulate the ambient vacuum environment. The nozzle axis was modeled with the symmetry condition. Finally, the secondary flow entering the annular portion of the duct was modeled with the fixed mass flow, total temperature, and flow angle. The secondary mass flow entered the cavity with a uniform velocity profile applied across the annular upstream boundary. For cases executed without secondary flow, the fixed mass-flow boundary condition was replaced with the no-slip condition.

C. Flowfield Parameters

The reference length for these simulations was specified as the nozzle throat diameter ($l_{\text{ref}} = 2.54$ cm). The ratio of specific heats was fixed at 1.2, and the constants for Sutherland's law were set according to values appropriate for steam. These values were chosen as representative of the combusting gaseous hydrogen and gaseous oxygen flow with an oxidizer-to-fuel ratio of six. The values were obtained by examining a series of one-dimensional equilibrium calculations[22] for the chamber conditions. The total temperature in the chamber was observed to increase slightly with increasing total pressure. The value of the gas constant was also observed to change a few percent over the pressure range of interest. This translates into a slightly different value of reference Reynolds number for each of the three chamber pressures considered. Thus the chamber conditions were specified as shown in Table 2. The Prandtl number was fixed at 0.6. The compositions of the primary and secondary flows were assumed to be equivalent. This was a constraint set by utilizing a single-species, calorically perfect-gas code, but nevertheless befits the assumption of a gas-generator-cycle engine. The secondary flow was injected at a constant total temperature of 1600°R.

D. Mesh Generation

Mesh generation was executed with Gridgen v11 software.[23] Several rules were observed for all of the different mesh geometries to ensure that similar spatial resolution was achieved for all cases:

1) Define the grid point clustering toward all no-slip surfaces with a near-wall spacing of 3.0×10^{-4} (l_{ref}).

2) Define maximum spacing away from surface not to exceed 0.25 (l_{ref}).

3) Define maximum stretching ratio of 1.2 between adjacent cells in any one dimension.

4) Utilize a three-block mesh topology with point-to-point interblock boundaries.

The price of adequate resolution was a large number of mesh points for the largest ducts (90,701). The important issue of documenting the mesh independence is addressed in the following section.

V. Statistical DOE

A. DOE and RSM

DOE is grounded in statistics and, thus, takes a radical departure from the typical Edisonian approach to experimentation. In the field of DOE, the primary objective is to effectively model the response of an experiment, as a function of the independent variables. Once the experiments are complete, an empirical model is constructed and can be optimized to meet overall objectives of reliability and performance. One advantage of this approach lies in the fact that optimum performance is not limited to the finite set of experimental responses gathered during experimentation. Rather, an optimum response usually exists in the design space at a region between the completed experiments. Prior to optimization, the final step in model construction involves validation of the empirical model. Successful prediction of a few additional experiments will build confidence in the empirical model. Of course, uncertainty analysis governs the reliability assessment of the empirical model. Therefore, reproducibility of the response must be quantified.

DOE strategies also have the advantage of minimizing the number of experiments, here CFD simulations, based on the complexity of the anticipated relationships between the response and the independent variables under investigation. In our specific situation the design complied with several other a priori restrictions.

1) The initial subset of nine CFD solutions should result in the formation of a multiple linear regression (MLR) model (hyperplane) for the purposes of comparing turbulence models and screening the independent variables to ensure their ranges were properly chosen.

2) The entire set of CFD solutions should result in the formation of an RSM model with linear, curvilinear, and two-way interaction terms.

3) The total number of required CFD solutions should result in a practical number of parametric experiments (i.e., <40).

The final design selected was a 36-case D-optimal[24] RSM model with an embedded multiple linear regression model. In other words the first nine CFD solutions permitted the estimation of a simple statistical model for general predictions of nozzle performance, and the full 36 solutions supported a higher-order model for accurate predictions of nozzle performance. The higher-order model contained an intercept [c_0], six linear terms [$c_1x_1, c_2x_2, \ldots, c_6x_6$], 15 bilinear or interaction terms [$c_7x_1x_2, c_8x_1x_3, \ldots, c_{21}x_5x_6$], and six curvilinear terms [$c_{22}x_1^2, c_{23}x_2^2, \ldots, c_{27}x_6^2$]. In practice, only the coefficients ($c_0, c_1, \ldots, c_{27}$), which are statistically significant (statistically different from zero), are retained in the final solution. Thus, DOE reduced the full parametric study (or full factorial) of 729 cases down to just 36. The final RSM model, once checked for adequacy of fit to the response data, was capable of predicting nozzle performance at any point within our six-dimensional design space without having to execute additional CFD simulations. The D-optimal design construction, MLR analyses, and RSM model analyses were executed with RS/1 software.[25] Detailed specification of the six independent variables for each case is presented in Table 3. Note that case 9 was the design centerpoint; each variable was set at the midlevel value.

Great care was taken to reduce potential sources of computational bias. Grid dependence, incomplete convergence, and numerical instability are all possible sources of bias in the response data that could potentially lead to false conclusions. Furthermore, unlike physical experimentation, repeating a CFD experiment should be exactly reproducible within machine accuracy. Hence, the typical MLR strategy of fitting a statistical model down to the level of experimental noise had to be abandoned. Instead, we fit the statistical model down to a level of uncertainty no less than $\pm 1\%$, to avoid overfitting the data. In other words, we expected to calculate an accurate representation of the governing model equations and report a response to within approximately $\pm 1\%$ uncertainty. In the next few sections we document the approach used to control these sources of computational bias and defend this assumed uncertainty estimate.

B. DOE and Mesh Dependence

A detailed mesh-convergence analysis was performed for the design centerpoint, case 9. This case was intentionally included as one of the 36 cases tested (from a possible matrix of 3^6 possibilities). It was a good candidate for detailed analysis because of its symmetric placement in our six-dimensional design space. The standard discretization of case 9 resulted in 56,952 points in the computational domain. A doubling of the grid in each direction results in a

Table 3 Thirty-six case experimental matrix: independent variable specification

	Independent variable settings					
Case	x_1 (P_c, psi)	x_2 ($\dot{m}_s \times 100\%/\dot{m}_p$)	x_3 (A_3/A^*)	x_4 (L/D_3)	x_5 (A_6/A_3)	x_6 (A_r/A^*)
1	300	8	39	2	2	4
2	300	0	39	5	2	20
3	1200	0	200	2	2	4
4	300	0	200	5	1	4
5	300	8	200	2	1	20
6	1200	8	200	5	2	20
7	1200	8	39	5	1	4
8	1200	0	39	2	1	20
9	750	4	120	3.5	1.5	12
10	300	0	200	2	2	20
11	1200	8	39	2	2	20
12	1200	0	200	5	1	4
13	1200	0	39	5	2	20
14	300	0	200	5	2	4
15	1200	8	200	5	1	20
16	300	8	200	2	2	4
17	300	8	39	5	2	20
18	1200	0	39	2	1	4
19	300	0	200	5	1	20
20	300	8	200	5	1	4
21	1200	8	39	5	2	4
22	1200	0	200	2	1	20
23	750	0	39	5	1	4
24	750	4	200	2	1	4
25	300	4	39	5	1.5	4
26	750	8	120	2	1.5	4
27	1200	0	200	5	1.5	12
28	300	4	120	5	1	12
29	300	8	39	3.5	1	4
30	300	0	120	2	1	4
31	300	4	39	2	1	20
32	1200	8	200	2	1	12
33	300	0	39	3.5	1.5	20
34	750	0	39	2	2	12
35	1200	8	39	5	1	20
36	1200	4	120	3.5	2	4

Table 4 Mesh dependence of I_{sp} for case 9

Parameter	Standard mesh	Fine mesh
# mesh point	56,952	226,281
I_{sp}, s	418.4	416.9
$\Delta\%$	0.346%	
GCI (β = 1.5)	1.6%	

quadrupling of the total points, to 226,281. The integral quantities changed very little, as evidenced by the data of Table 4.

The mesh-dependence data were presented in terms of a net difference and the standard grid-convergence index (GCI).[26] The unique advantage of reporting the GCI value lies in the uniform manner of presenting dependent variable changes. The GCI is not a bound on the error; rather it is "...a reasonable error band, in the flavor of a statistician's 2σ range or an experimentalist's 20:1 odds...".[25] The GCI is calculated with the following formula:

$$\mathrm{GCI} = \frac{3(\Delta\%)\alpha^{\beta}}{(\alpha^{\beta} - 1)} \tag{4}$$

where α is the grid-refinement ratio and β is the numerical order of accuracy of the CFD solver. For our study, $\alpha = 2$ and conservatively estimating the spatial accuracy of the CFD between first and second order, we set $\beta = 1.5$. The GCI value was 1.6%. Thus, we assume that the standard approach to mesh generation just outlined has removed any significant mesh dependence of the I_{sp} results upon which our statistical model is based.

The local flow properties of wall static pressure and centerline Mach number, shown in Fig. 2, revealed noticeable mesh dependence in the solution of case 9. This does not, however, contradict the data of Table 4. One would expect integral properties to exhibit less sensitivity to mesh refinement than local properties, and thus reach an asymptotic value earlier in a mesh-refinement study. This is particularly true for local properties in the neighborhood of strong gradients such as shock and contact surfaces. We have included the data of Fig. 2 to highlight an important observation: different aspects of a given CFD simulation reach mesh independence at different levels of mesh refinement. Mesh-refinement analysis must be carried out upon the specific response data of interest. Clearly a response surface model build upon local centerline Mach-number data would require further mesh refinement to avoid an unacceptable level of bias/uncertainty caused by inadequate spatial resolution.

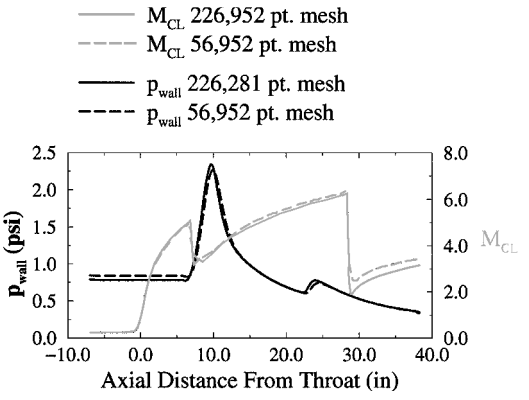

Fig. 2 Mesh dependence: centerline Mach number and mixer-ejector surface pressure for case 9.

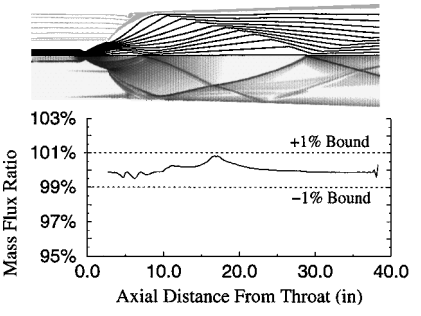

Fig. 3 Mass-flux ratio vs axial location, plotted from the rocket exit plane to the mixer-ejector exit plane for case 9.

C. DOE and Iterative Convergence

At the outset, we addressed the issue of the reported values of I_{sp} and their sensitivity to incomplete iterative convergence. Often overlooked, this issue proved to be nontrivial when considering DOE and CFD. The residuals of mass flow and thrust converged at least four orders of magnitude. Furthermore, we demanded that the value of I_{sp} should not change more than 0.15% over the last 10,000 iterations at a Courant number of 0.5. This criterion required several of the longest domains to be run in excess of 50,000 iterations, depending upon the initial conditions prescribed. The extremely long iteration counts were necessary to resolve the widely varying wave speeds present in a domain with large regions of low-speed flow present alongside hypersonic jet flow. Figure 3 illustrated the small variation of integrated mass flux as a function of axial location for the converged result of design centerpoint, case 9. The mass-flux ratio of Fig. 3 was simply the local integrated mass flux, normalized by the average integrated mass flux. We assume that the preceding approach for convergence analysis has removed any significant iterative dependence of the I_{sp} results upon which our statistical model is based.

D. DOE and Artificial Dissipation

For most of the 36 cases, the coefficients of second- and fourth-order artificial viscosity were fixed at $\frac{1}{4}$ and $\frac{1}{100}$, respectively.

However, for some of the configurations involving the largest primary rocket nozzles, numerical stability became an issue. Convergence of the exit mass flux and thrust were oscillating such that I_{sp} varied as much as $\pm 1.5\%$ instead of converging toward machine accuracy. We found that specifying the coefficient of fourth-order diffusion at a value of $\frac{1}{32}$ was sufficient to stabilize the flowfield without altering the I_{sp} integrals significantly. All of the cases run with the elevated fourth-order artificial diffusion had I_{sp} values that converged within the band of oscillation already observed. No adjustment to the second-order artificial diffusion coefficient was needed for any of the 36 cases.

To be complete about assessing the effects of elevated fourth-order artificial diffusion, we decided to examine a case that did not suffer from numerical instability. The design centerpoint was a good candidate for the reasons just mentioned. When the CFD simulation of case 9 was repeated with the higher coefficient of fourth-order artificial diffusion, the I_{sp} value changed from a converged value of 418.36 to 419.65 or 0.30%. Thus, we assume that the modification of fourth-order diffusion just outlined has removed the uncertainty associated with numerical stability without compromising the I_{sp} results upon which our statistical model is based.

VI. Results

A. RBCC Nozzle Flowfield

A few dominant flow features were common to all RBCC nozzles we have examined. A brief examination of these phenomena provided for a more complete interpretation of the statistics. Figure 4 is a composite picture of the design centerpoint, case 9. The upper half of the figure is a numerical schlieren image, and the lower half is a plot of iso-Mach contours. The numerical schlieren image was based upon a transformation of the calculated density gradient.[27] It was particularly helpful in revealing the presence of expansion fans, shock waves, and shear layers.

In the following discussion, we will refer to the expansion within the RBCC nozzle in three stages, shown in Fig. 4. The first or primary stage of expansion occurred within the contoured rocket nozzle. The second or free expansion, occurred between the rocket exit and mixer-ejector wall. The third, or duct expansion, occurred within the diverging mixer-ejector.

Two different compression phenomena were observed. A continuous series of weak compression waves were visible within all three of the Rao-optimized[28] rocket nozzles studied. Also note that a plume shock formed downstream of the rocket nozzle exit and always reflected off of the duct wall. For elongated mixer-ejector geometries the plume shock was seen to reflect several times between the duct wall and centerline.

B. Flow Visualization

The primary expansion was governed by the rocket nozzle geometry. This nozzle contour was optimized with the Rao algorithm.

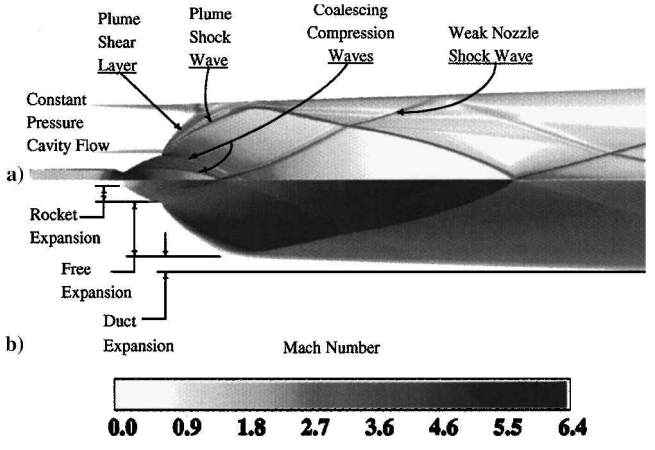

Fig. 4 Composite image of design centerpoint, case 9: a) numerical schlieren image and b) computed Mach-number contours.

A perfect nozzle contour balanced the expansion and compression waves generated at the cost of excessive nozzle length. A Rao contour shortened the nozzle length while maximizing the thrust generated. The cost of this optimization was the generation of weak compression waves from the contoured nozzle. These compression waves were present within all three of our Rao-contoured nozzles and were visible in Fig. 4. The compression waves originated at the nozzle wall and coalesced at some point downstream of the rocket nozzle exit plane. It appeared that these weak waves had begun to coalesce along the upstream edge of the compression and fully coalesced after reflecting off of the centerline.

The free expansion revealed a structure similar to an underexpanded supersonic free jet. A high-speed shear layer surrounded the primary plume shock. The shape of this high-speed shear layer was a function of the rocket nozzle exit pressure and the static pressure of the annular cavity region. This high-speed shear layer defined the boundary between the fast moving plume flow and the slow (or stagnant) cavity flow. Because the shear layer was a constant pressure process, its location was a function of the cavity pressure.

The static pressure of the annular cavity was dependent upon the cross-sectional area and the magnitude of secondary flow injected. Secondary flow injection also had an important effect in the stagnation region of the shear layer. Consider the pictures of cases 20 and 4 shown in Fig. 5. The only difference between these two simulations was the presence of 8% secondary flow injected into the annular cavity. Note the different locations of the primary shear layers and shock waves. An examination of the peak static pressure along the duct wall (Fig. 6) revealed that the primary shock wave impinged further downstream in the presence of secondary flow injection. The impingement point of case 20 was nearly twice that of case 4, when measured from the rocket exit plane. This relates directly to the compression necessary to turn the flow toward the axial direction.

Figure 5 also dramatically illustrated the impact that injected secondary flow had upon the development of streamline patterns inside

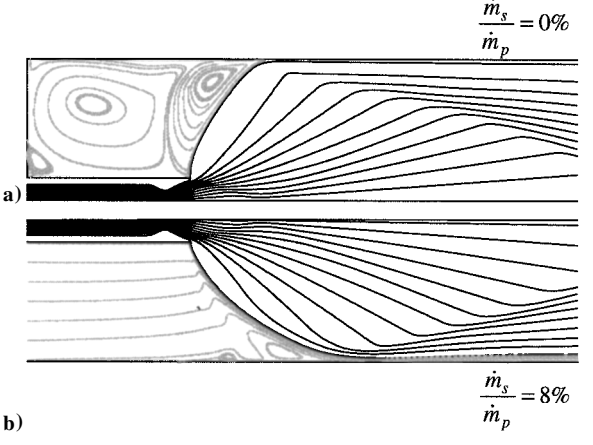

Fig. 5 Particle traces: gray represents the secondary flow streaklines; black represents the primary flow streaklines for a) no injected flow (case 4) and b) 8% injected flow (case 20).

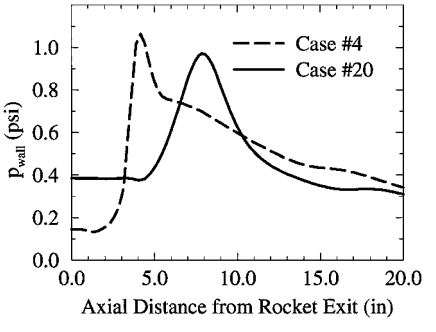

Fig. 6 Mixer-ejector surface pressure comparison; notice the effect of secondary flow upon the peak pressure (shock impingement).

Table 5 Tabulation of the I_{sp} data from all of the CFD simulations

Case	I_{sp}^{MAX}	Calculated I_{sp}^{CFD}		Calculated $\eta_{I_{sp}}^{CFD}$	
		k–ε	SA	k–ε, %	SA, %
1	451.57	410.42	399.54	90.89	88.48
2	451.57	427.06	424.33	94.57	93.97
3	480.04	415.88	415.94	86.63	86.65
4	465.06	373.85	361.73	80.39	77.78
5	465.06	425.22	411.29	91.43	88.44
6	480.04	437.21	430.64	91.08	89.71
7	445.44	375.30	374.07	84.25	83.98
8	445.44	418.70	416.89	94.00	93.59
9	468.03	423.38	418.36	90.46	89.39
10	473.31	——	433.80	——	91.65
11	457.99	——	425.32	——	92.87
12	471.67	——	375.90	——	79.69
13	457.99	——	432.92	——	94.53
14	473.31	——	393.85	——	83.21
15	471.67	——	415.28	——	88.04
16	473.31	——	407.86	——	86.17
17	451.57	——	412.17	——	91.28
18	445.44	——	376.14	——	84.44
19	465.06	——	403.11	——	86.68
20	465.06	——	372.02	——	79.99
21	457.99	——	399.24	——	87.17
22	471.67	——	419.26	——	88.89
23	443.34	——	369.83	——	83.42
24	469.45	——	381.15	——	81.19
25	446.71	——	384.22	——	86.01
26	468.03	——	404.67	——	86.46
27	476.73	——	415.05	——	87.06
28	458.00	——	397.36	——	86.76
29	439.19	——	377.51	——	85.96
30	458.00	——	369.02	——	80.57
31	439.19	——	399.86	——	91.04
32	471.67	——	415.49	——	88.09
33	446.71	——	419.92	——	94.00
34	455.83	——	427.36	——	93.76
35	445.44	——	401.40	——	90.11
36	473.98	——	404.55	——	85.35

the annular cavity region. If the cavity was closed ($\dot{m}_s/\dot{m}_p = 0$), then the secondary flowfield was essentially a supersonic driven cavity. Case 4 developed two large recirculating zones and several smaller ones. A substantial shear layer between the two large eddies was visible in many of the schlieren images of closed cavities. Case 20, however, developed one small eddy near the primary shock impingement. Otherwise, the secondary flow was sent downstream along the duct wall.

The third stage of expansion occurred inside the mixer-ejector only when divergence was present ($A_6/A_3 > 0$). Oblique shock waves often reflected at the jet centerline and the mixer-ejector wall. The shock-wave/boundary-layer interaction often resulted in flow separation and reattachment. For these cases an oblique shock formed off the front and back sides of the larger separation bubbles. This complex behavior is well known to occur for hypersonic shock-wave/boundary-layer interactions.[29]

C. Calculated Nozzle Efficiency

We shall begin by presenting the tabulation of the I_{sp} data, from all of the CFD simulations, in Table 5. The first nine cases were executed twice, once with each of the turbulence models under consideration. This allowed an independent regression analysis for each turbulence model. Analysis of variance techniques were applied to determine if the differences between the two turbulence models were statistically significant. Cases 10–36 were calculated with the S-A turbulence model only. The entire 36 case data set using S-A was used to build the full RSM model described next.

D. Multiple Linear Regression Analysis: Cases 1–9

Both MLR analyses of the two turbulence models agreed upon the significance and magnitude of four linear effects. Primary rocket area ratio and mixer-ejector exit area exhibited a positive linear relationship with $\eta_{I_{sp}}$. Mixer-ejector inlet area and mixer-ejector length/diameter ratio exhibited a negative linear relationship with $\eta_{I_{sp}}$. However, the secondary flow and chamber pressure did not appear to have a significant effect upon nozzle efficiency for either turbulence model.

The analysis of variance revealed a small, albeit statistically, significant difference between the two turbulence models' predictions. This difference was in the magnitude of the intercept value; k–ε model coefficient was approximately 1% greater. This simply indicated that the k–ε model tended to predict a slightly higher level of nozzle efficiency. We interpreted this to indicate that the choice between these two turbulence models would not affect the relative prediction of the regression, but would slightly influence the absolute prediction. This can be confirmed by briefly examining the slightly higher efficiencies shown for k–ε in Table 5. A lengthy description of these linear regression results has been omitted in favor of concentrating upon the more complete RSM results. The interested reader is referred to a companion paper.[18]

The preceding MLR analysis was available to us before the completion of cases 10–36. As a result, we chose to use the S-A model instead of the k–ε model to complete the study for the following reasons: 1) faster iterative convergence, 2) more robust performance for our configurations, and 3) statistically similar efficiency predictions. Therefore, all solutions discussed from here on will refer to the S-A model results.

At this point the MLR analysis produced a model, which revealed that nozzle efficiency varied linearly with four different parametric effects. However, the MLR analysis had to assume that neither curvature nor interaction existed in this regression. This was an intrinsic assumption from the chosen nine-experiment DOE. We felt that these effects might actually be present because so much of fluid analysis is truly nonlinear. One hint of the nonlinearity lurking in the results was given by comparing the MLR-predicted efficiencies with the actual CFD values for the first nine cases. This revealed that the linear model fit the CFD data at the edges of design space better than at the center. This can imply curvature in the data, not accounted for in the simple regression model. Another concern involved the fact that we had fit a five-term model (intercept and four linear terms) using nine CFD simulations. This leaves us with just four extra degrees of freedom in the regression error, a statistical entity used to access model adequacy. By completing the full 36 cases, we directly addressed the question of nonlinearity while gaining more degrees of freedom in the statistical model's error term.

E. Response Surface Model Analysis: Cases 1–36

As expected, the response surface model revealed many more significant effects than the simpler linear regression analysis. In total, 13 separate model coefficients were considered significant in the RSM analysis [Statistically, the model coefficients are either significantly different than zero (i.e., greater than 95% significant), or assumed to be zero.]; the model coefficient values and significance levels are given in Table 6. For the purposes of the following discussion, the model terms of the form $\hat{x}_i$ will be referred to as linear, $\hat{x}_i\hat{x}_j$ as bilinear, and $\hat{x}_i^2$ as curvilinear. The statistical model to predict RBCC system efficiency was defined by Table 1, Eq. (1), and Table 6. It is given in Eq. (5):

$$\begin{aligned}\eta_{I_{sp}}^{RSM} &= (89.325) + (0.3503)\hat{x}_1 - (1.6150)\hat{x}_3 - (0.6976)\hat{x}_4 \\ &+ (1.6077)\hat{x}_5 + (3.2062)\hat{x}_6 + (0.3344)\hat{x}_1\hat{x}_3 \\ &+ (0.3626)\hat{x}_2\hat{x}_3 - (0.4209)\hat{x}_2\hat{x}_5 - (0.7228)\hat{x}_2\hat{x}_6 \\ &+ (0.2830)\hat{x}_3\hat{x}_5 - (0.4061)\hat{x}_5\hat{x}_6 - (1.5860)\hat{x}_6^2 \end{aligned} \quad (5)$$

An approximate prediction error and specified confidence interval can be calculated for this RSM. This error estimate is based upon the root-mean-squared error of the regression and Student's t-distribution. The 95% confidence predictive uncertainty associated with the RSM model was approximately ($\pm 1.1\%$).

Although Eq. (5) provided a means for quantitative examination of our RSM model, graphical interpretation was far more useful for

Table 6 RSM model coefficient values and significance

RSM model term	Coefficient	Significance, %
1	89.325	99.99
$\hat{x}_1$	0.3503	99.16
$\hat{x}_2$	0.0	——
$\hat{x}_3$	−1.6150	99.99
$\hat{x}_4$	−0.6976	99.99
$\hat{x}_5$	1.6077	99.99
$\hat{x}_6$	3.2062	99.99
$\hat{x}_1\hat{x}_2$	0.0	——
$\hat{x}_1\hat{x}_3$	0.3344	98.46
$\hat{x}_1\hat{x}_4$	0.0	——
$\hat{x}_1\hat{x}_5$	0.0	——
$\hat{x}_1\hat{x}_6$	0.0	——
$\hat{x}_2\hat{x}_3$	0.3626	98.89
$\hat{x}_2\hat{x}_4$	0.0	——
$\hat{x}_2\hat{x}_5$	−0.4209	99.53
$\hat{x}_2\hat{x}_6$	−0.7228	99.99
$\hat{x}_3\hat{x}_4$	0.0	——
$\hat{x}_3\hat{x}_5$	0.2830	95.53
$\hat{x}_3\hat{x}_6$	0.0	——
$\hat{x}_4\hat{x}_5$	0.0	——
$\hat{x}_4\hat{x}_6$	0.0	——
$\hat{x}_5\hat{x}_6$	−0.4061	99.45
$\hat{x}_1^2$	0.0	——
$\hat{x}_2^2$	0.0	——
$\hat{x}_3^2$	0.0	——
$\hat{x}_4^2$	0.0	——
$\hat{x}_5^2$	0.0	——
$\hat{x}_6^2$	−1.5860	99.99

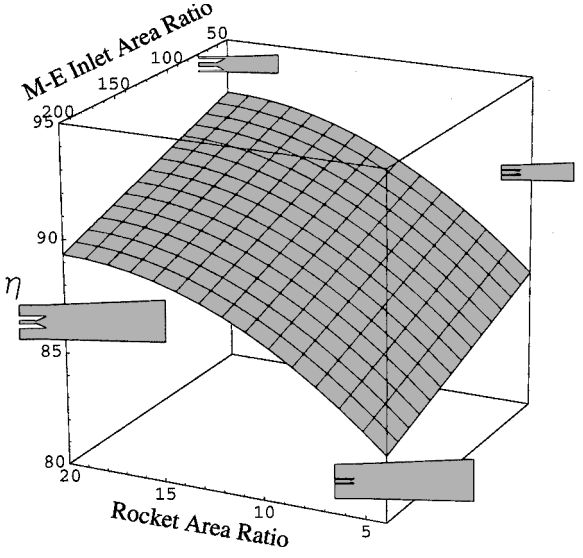

Fig. 7 Efficiency η as a function of mixer-ejector inlet area ratio (A_3/A^*) and rocket area ratio (A_r/A^*).

exploring the results. Each of the following sections begins with a three-dimensional carpet plot of the efficiency, followed by a discussion of the physical implications. For each carpet plot, efficiency was portrayed along the vertical axis as a function of two independent variables. Unless otherwise noted, the remaining independent variables are set to their respective midlevel values.

1. Annular Cavity Size

The carpet plot of efficiency η as a function of rocket area ratio (A_r/A^*) and mixer-ejector inlet area ratio (A_3/A^*) revealed a large part of our story. This carpet plot, shown in Fig. 7, portrayed efficiency as a function of two geometric variables. Thus each point on the surface corresponded to a slightly different geometry, with the limiting configurations shown in two-dimensional silhouette at the four corners. This surface was curvilinear because of the quadratic influence of rocket area ratio (i.e., term $\hat{x}_6^2$). Also note that the four corner points are coplanar, evidence that no interaction occurs between these variables.

Examination of Fig. 7 highlighted two important features: 1) an increase in rocket area ratio corresponded to an increase in performance, and 2) a decrease in mixer-ejector inlet area ratio led to an increase in performance. Consequently, the maximum performance shown on this surface occurred for the configuration ($A_r/A^* = 20$) and ($A_3/A^* = 50$). The physical implication of these two observations was consistent: reduce the size of the annular cavity region to improve the efficiency. Recall that reduction of the annular cavity corresponds to a reduction of the free-expansion portion of the flow. These observations lead to the suspicion that free expansion across the annular cavity was an inefficient process, when compared to the attached expansions within the Rao nozzle and the mixer-ejector. Further analysis of the CFD data confirmed this suspicion.

To measure the thrust achieved during the free expansion, we integrated the static pressure in the annular cavity across the upstream wall. However, this method of calculating the free-expansion thrust was strictly valid for the subset of cases with straight mixer-ejectors and no injected secondary flow. The calculated free-expansion thrust was then compared with the isentropic value expected from an area increase of (A_r/A^*) to (A_3/A^*). The ratio of these two values of thrust can be expressed as the efficiency of free expansion. Typical free-expansion efficiency values were between 20–30%, depending on the specific geometry. This was in sharp contrast to the Rao-optimized rocket nozzle expansions, which registered above 95% efficient for all cases. Static pressure observed within the cavity was essentially constant behind the high-speed shear layer. This observation agreed with the data of Fortini.[7]

We believe that the losses associated with the large free expansion are caused primarily by overexpansion. We have already noted that the cavity pressure drops below the value predicted by isentropic flow, which caused the expanding flow to exit the rocket nozzle at a steeper angle than anticipated. This required a stronger oblique shock structure to turn the flow toward the axial direction, and ultimately led to a more intense stagnation flow at the duct wall. Examine the flowfield of case 4 depicted in Fig. 5. Notice how steeply the plume expanded in the radial direction, downstream of the rocket nozzle exit.

2. Mixer-Ejector Divergence

The carpet plot of efficiency η as a function of mixer-ejector inlet area ratio (A_3/A^*) and exit area ratio (A_6/A_3) revealed another important part of our study. Figure 8 clearly shows that increasing mixer-ejector exit area ratio substantially improved the

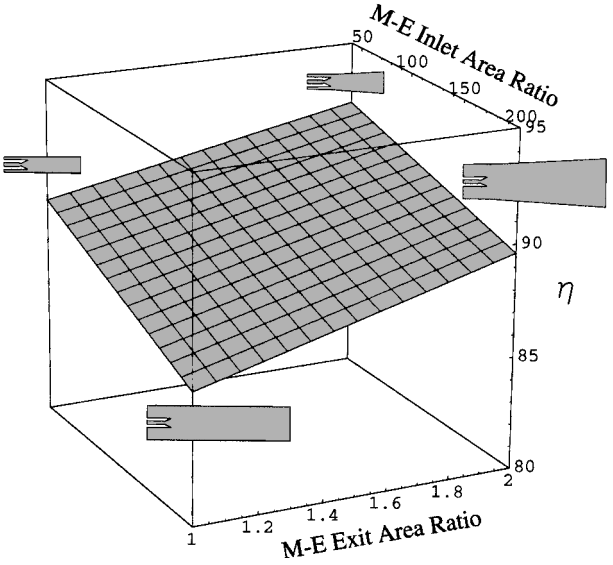

Fig. 8 Efficiency η as a function of mixer-ejector inlet area ratio (A_3/A^*) and mixer-ejector exit area ratio (A_6/A_3).

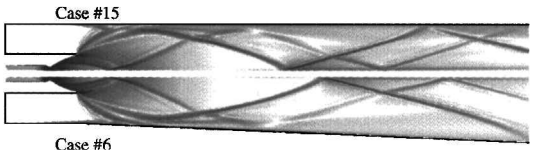

Numerical schlieren image

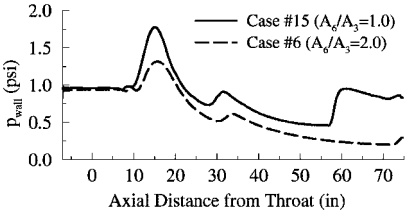

Mixer-ejector surface-pressure comparisons

Fig. 9 Effect of mixer-ejector divergence.

performance. Again, we see that decreasing the mixer-ejector inlet area improved performance. For the configurations shown in Fig. 8, the maximum efficiency occurred in the corner where $(A_3/A^* = 50)$ and $(A_6/A_3 = 2)$.

Increasing (A_6/A_3) to a value greater than unity was tantamount to introducing divergence into the mixer-ejector geometry. This divergence improved the efficiency for two reasons. Divergence caused an efficient attached-expansion to occur within the mixer-ejector. Divergence also caused the plume shock to reflect at a shallower angle, which delayed the onset of boundary-layer separation downstream. These effects were visible in the comparison of cases 6 and 15 in Fig. 9. The physical implications were consistent with that just discussed. Namely, the efficiency was maximized when the influence of free-expansion losses was reduced as much as possible.

The slope of the response surface of Fig. 8, with respect to (A_6/A_3), was a function of (A_3/A^*). In other words, the slope of this carpet plot $[\partial\eta(\hat{x}_3, \hat{x}_5)/\partial\hat{x}_5]_{\hat{x}_1,\hat{x}_2,\hat{x}_4,\hat{x}_6=0}$ depended upon the value of $(\hat{x}_3)$. This was caused by the interaction between these two variables, or term $\hat{x}_3\hat{x}_5$ of Eq. (5). In fact, the slope of the six-dimensional response surface with respect to $\hat{x}_5$ depended upon the values of $\hat{x}_2$, $\hat{x}_3$, $\hat{x}_6$, caused by three separate bilinear interactions. Despite the seeming complexity of variable interactions, the following observations can be made: 1) the surface gradients of Fig. 8 were largest near the configuration with minimum efficiency, and 2) the free-expansion losses were maximized for the same configuration because of the large mixer-ejector inlet ratio and no mixer-ejector divergence. Thus, the variable interaction corroborated our earlier evidence.

3. *Rocket Area Ratio and Mixer-Ejector Divergence*

The carpet plot of efficiency η as a function of rocket area ratio (A_r/A^*) and mixer-ejector exit area ratio (A_6/A_3) revealed the third major part of the results. Figure 10 confirmed what we have already observed from Figs. 7 and 8: 1) increasing (A_r/A^*) improved efficiency and 2) increasing (A_6/A_3) also improved efficiency. Again, the quadratic effect of rocket area ratio upon performance was revealed in the curvilinear surface plot. However, the two quadratic curves that bound this surface were different, because of the variable interaction. Thus, this surface plot has curvature because of the term $\hat{x}_6^2$ and twist caused by the bilinear term $\hat{x}_5\hat{x}_6$.

We have already discussed the influence of both (A_r/A^*) and (A_6/A_3) upon the efficiency. However, the variable interaction $\hat{x}_5\hat{x}_6$ was not visible from Figs. 7 and 8. We can see from Fig. 10 that the configuration with the largest annular cavity and no mixer-ejector divergence offered the least efficient performance. Consequently, this configuration stood to gain the most by increasing (A_r/A^*) and/or increasing (A_6/A_3). Thus, the largest surface gradients are located in this corner of the carpet plot and gradually decrease in magnitude until the most efficient configuration was achieved. The variable interaction $\hat{x}_5\hat{x}_6$ was evidence of this phenomenon.

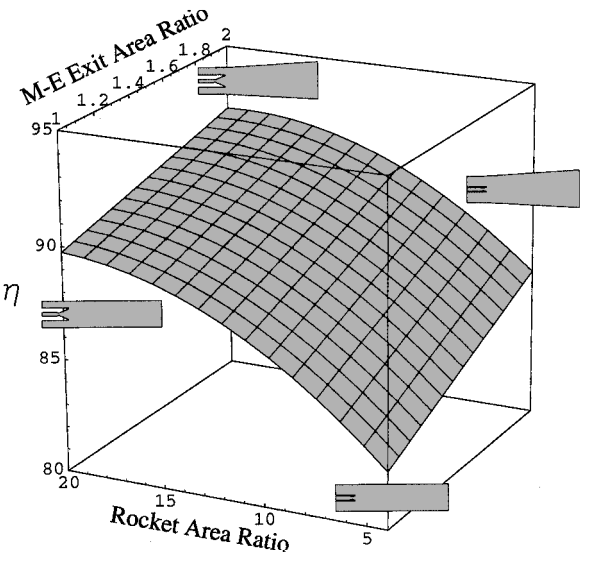

Fig. 10 Efficiency η as a function of mixer-ejector exit area ratio (A_6/A_3) and rocket area ratio (A_r/A^*).

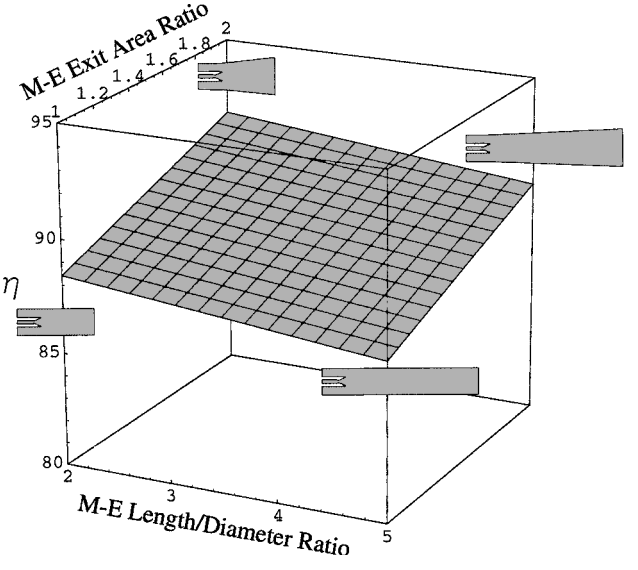

Fig. 11 Efficiency η as a function of mixer-ejector length/diameter ratio (L/D_3) and mixer-ejector exit area ratio (A_6/A_3).

4. *Mixer-Ejector Length*

The carpet plot of efficiency as a function of mixer-ejector exit area (A_6/A_3) and length/inlet diameter (L/D_3) ratios was quite interesting. Figure 11 clearly shows the small influence that mixer-ejector length had upon efficiency. Extending (L/D_3) from two to five resulted in a few percent reduction of efficiency. We attributed this to the drag resulting from increased wetted surface area within the mixer-ejector. Notice that for a given (L/D_3), increasing (A_6/A_3) resulted in a net gain in efficiency, despite the increase in wetted area. The key point to emphasize here is that by increasing the duct exit area we diluted the free-expansion losses by including an additional attached expansion within the mixer-ejector. On the other hand, a simple extension of the mixer-ejector geometry merely added drag to the system, without any increase in thrust. The response surface of Fig. 11 was a simple plane without any variable interaction.

5. *Secondary Flow Injection*

Recall Fig. 7, which displayed the efficiency as a function of mixer-ejector inlet area ratio (A_3/A^*) and rocket area ratio (A_r/A^*). We observed that maximizing (A_r/A^*) was important along with minimizing (A_3/A^*). Secondary flow $(\dot{m}_s/\dot{m}_p)$ had an interacting

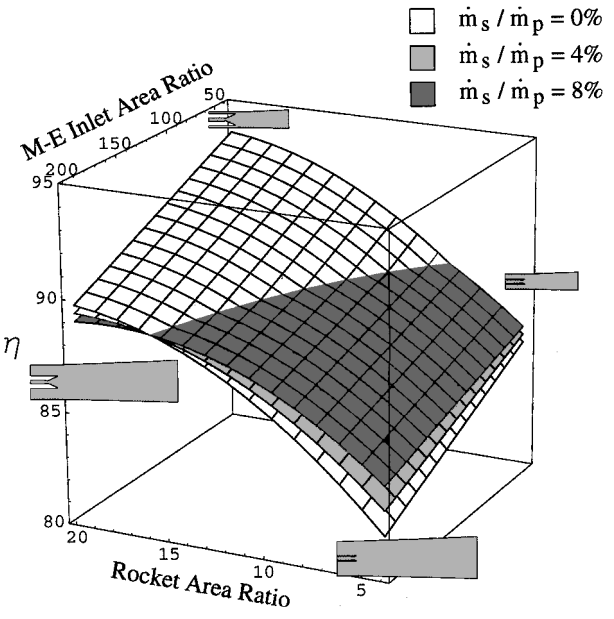

Fig. 12 Efficiency η as a function of mixer-ejector inlet area ratio (A_3/A^*) and rocket area ratio (A_r/A^*): interaction of secondary flow ($\dot{m}_s/\dot{m}_p$).

effect with both of these parameters, as seen from the terms $\hat{x}_2\hat{x}_3$ and $\hat{x}_2\hat{x}_6$ in Eq. (5).

Figure 12 displays the effect of three different values of ($\dot{m}_s/\dot{m}_p$). The gray surface, similar to that plotted in Fig. 7, corresponded to the midlevel of ($\dot{m}_s/\dot{m}_p = 4\%$); the white surface corresponded to ($\dot{m}_s/\dot{m}_p = 0\%$); and the dark surface corresponded to ($\dot{m}_s/\dot{m}_p = 8\%$). Plotting all three surfaces together highlighted the influence of secondary flow upon the effects of these two variables. The extrema of performance were altered by secondary flow injection, but in opposite ways. The performance of the most efficient configuration was maximized without injecting any secondary flow. However, increasing the secondary flow injection to 8% maximized the performance of the least efficient configuration. Secondary flow injection into the annular cavity must have helped to relieve the free-expansion losses, but at an overall system cost.

We suspect that the benefit of secondary flow derived from the increased static pressure within the cavity. This had the effect of reducing the free expansion, thereby reducing both the expansion angle and the strength of the reflected plume shock. There was also a direct contribution to stream thrust from secondary flow injection, although the I_{sp} of this secondary flow was dependent upon the precise configuration. We suspect that injection of secondary flow, with a lower total pressure, into the mixer-ejector was a competing loss mechanism. The cost-benefit analysis of secondary flow injection appeared to rest on the significance of the free-expansion losses, which were geometry specific. We also suspect that a different composition of the secondary flow may alter the balance of these competing effects.

Secondary flow had an interactive effect with mixer-ejector exit area ratio also. This effect was quite similar to that shown in Fig. 12, in that the extrema of performance were affected. From Figs. 8 and 10, we have shown that performance increased when the mixer-ejector exit area was maximized. We surmised that the free-expansion losses were most significant for mixer-ejectors without divergence ($A_6/A_3 = 1$). Thus we might expect that maximizing secondary flow injection would improve performance for mixer-ejectors with minimum divergence and likewise reduce performance for mixer-ejectors with maximum divergence. This was precisely what occurred.

F. Results Summary

1) Attached expansions within the rocket nozzle and mixer-ejector duct were far more efficient than free-expansion across the annular cavity.

Table 7 Confirmation runs to examine the bilinear interaction ($c_{14}x_2x_5$) (Note that x_1, x_3, x_4, and x_6 are fixed at their mean values.)

Case	x_2 ($\dot{m}_s/\dot{m}_p$), %	x_5 (A_6/A_3)	$\eta_{I_{sp}}^{CFD}$, %	$\eta_{I_{sp}}^{RSM}$, %	Δ, %
37	0	2	89.94	91.35	−1.41
38	0	1	86.98	87.30	−0.32
39	8	2	89.65	90.51	−0.86
40	8	1	87.58	88.14	−0.56

Table 8 Confirmation runs to examine the bilinear interaction ($c_{15}x_2x_6$) (Note that x_1, x_3, x_4, and x_5 are fixed at their mean values.)

Case	x_2 ($\dot{m}_s/\dot{m}_p$), %	x_6 (A_r/A^*)	$\eta_{I_{sp}}^{CFD}$, %	$\eta_{I_{sp}}^{RSM}$, %	Δ, %
41	0	20	91.29	91.67	−0.38
42	0	4	83.46	83.81	−0.35
43	8	20	89.69	90.22	−0.53
44	8	4	85.39	85.26	0.13

2) Nozzle efficiency was improved when the size of the annular cavity was reduced by increasing the rocket exit area ratio (A_r/A^*) and reducing the mixer-ejector inlet area (A_3/A^*).

3) Mixer-ejector expansion, present when ($A_6/A_3 > 1$), generally improved efficiency by efficiently expanding the flow within the mixer-ejector and reducing the losses associated with the reflecting plume shock.

4) Nozzle efficiency was inversely proportional to the overall length of the mixer-ejector duct; this was a relatively minor effect.

5) Secondary flow injection ($\dot{m}_s/\dot{m}_p$) could mitigate free-expansion losses, although at some overall cost, through variable interactions: relatively inefficient configurations, with large free-expansion regions, benefited from maximizing ($\dot{m}_s/\dot{m}_p$) and relatively efficient configurations, with small free-expansion regions, benefited from minimizing ($\dot{m}_s/\dot{m}_p$).

6) Statistically significant bilinear and curvature terms underscored the importance of executing the full 36-case D-optimal design versus the simple nine-case MLR design.

VII. RSM Confirmation

The final step in DOE involved the execution of confirmation tests. These additional computations tested the overall ability of the RSM model to predict RBCC nozzle efficiency integrated from CFD simulation. However, the eight new cases were chosen to specifically assess the validity of the two largest bilinear interactions $\hat{x}_2\hat{x}_5$ and $\hat{x}_2\hat{x}_6$. Cases 37–40 were configured to address the former bilinear interaction, and cases 41–44 addressed the latter, as shown in Tables 7 and 8. All but case 37 were well within the approximate uncertainty band of (±1%). Case 37 results lay just outside the uncertainty band.

VIII. Conclusions

The present computational effort represents an essential first step in assessing the performance of RBCC systems during all-rocket mode operation. We have utilized a statistical design of experiments approach to quantify the influence of four geometric and two flowfield variables using Reynolds-averaged Navier–Stokes analysis. A D-optimal parametric matrix was selected, and 36 separate CFD simulations were included in a full RSM model of RBCC nozzle performance, based on I_{sp} efficiency. RBCC nozzle performance ranged between 77–95% efficient.

Numerical flow visualization was used extensively to reveal some of the underlying physics behind the statistical results. Several interesting fluid phenomena have been identified for further research. It is apparent that the free-expansion process, directly downstream of the rocket nozzle, influenced the overall RBCC nozzle performance. Maximizing the efficiency of this free expansion will demand some creative design solutions.

A response surface model of RBCC nozzle performance was developed, with 13 significant terms affecting the shape and flow conditions of a generic RBCC system. Predictions of system efficiency can now be made throughout our continuous, six-dimensional

design space, without the need for further CFD simulations. Prediction accuracy to within approximately (±1%) of a similar CFD simulation is expected, with 95% confidence. This uncertainty estimate appears to be valid, in light of the eight additional confirmation tests completed. This model can now be used in system design and analysis for RBCC propulsion optimization.

Finally, the cornerstone of the present work was the incorporation of CFD into the framework of statistical DOE. The D-optimal experimental design provided a parametric matrix of CFD simulations that efficiently explored the six-dimensional design space. We assert that a comprehensive approach to uncertainty/bias estimation was incorporated into the present computational study. We have confined our discussion of simulation uncertainty/bias to the issue of verification, or accurate representation of the governing model equations. The statistical framework of DOE focused our analysis upon the interpretation of statistically significant results, using this uncertainty estimate as the discriminator. Flow parameters integrated from the CFD solution (such as mass flow, thrust, and specific impulse) appear to be particularly well suited to the regression techniques of response surface models.

Acknowledgments

The authors would like to acknowledge the following colleagues for their insight during preparation of this document: D. R. Reddy, M. D. Klem, C. J. Trefny, and R. V. Chima.

References

[1]Escher, W. J. D., and Flornes, B. J., "A Study of Composite Propulsion Systems for Advanced Launch Vehicle Applications," Marquardt Co. Rept. 25,194 for NASA Contract NAS7-377, Vol. 1–7, Sept. 1966.

[2]Daines, R. L., and Merkle, C. L., "Computational Fluid Dynamic Modeling of Rocket-Based Combined-Cycle Engine Flowfields," AIAA Paper 94-3327, June 1994.

[3]Foster, R. W., "Optimization of the Rocket Mode Trajectory in a Rocket-Based Combined-Cycle (RBCC) Engine Powered SSTO Vehicle," AIAA Paper 89-2295, July 1989.

[4]NASA Office of Public Affairs, "NASA Selects Five Organizations to Develop Technologies for an Air Breathing Rocket Engine," Press Release HQ 96-135, 11 July 1996.

[5]Olds, J. R., and Lee, H., "Application of a New Economic Analysis Tool to a Two-Stage-to-Orbit RBCC Launch Vehicle Design," AIAA Paper 96-4092, Sept. 1996.

[6]Olds, J. R., "Results of a Rocket-Based Combined-Cycle SSTO Design Using Parametric MDO Methods," Society of Automotive Engineers, Paper 941165, April 1994.

[7]Fortini, A., "Performance Investigation of a Non-Pumping Rocket-Ejector System for Altitude Simulation," NASA TN D-257, Dec. 1959.

[8]Korst, H. H., "Theory for Base Pressures in Transonic and Supersonic Flow," *Journal of Applied Mechanics*, Vol. 23, No. 4, 1956, pp. 593–600.

[9]Petrie, H. L., Samimy, M., and Addy, A. L., "A Study of Compressible Separated Flows," *AIAA Journal*, Vol. 24, No. 12, 1986, pp. 1971–1978.

[10]NPARC Alliance Technical Team, "NPARC User's Guide, Version 3.0," Tullahoma, TN, Sept. 1996.

[11]Cooper, G. K., Garrard, G. D., and Phares, W. J., "PARC Code Validation for Propulsion Flows," Arnold Engineering Development Center, TR-88-32 (AD-A204293), Tullahoma, TN, Jan. 1989

[12]Garrard, G. D., Phares, W. J., and Cooper, G. K., "Calibration of PARC for Propulsion Flows," AIAA Paper 91-2152, June 1991.

[13]Mead, R., *The Design of Experiments: Statistical Principles for Practical Application*, Cambridge Univ. Press, Cambridge, Great Britain, U.K., 1988.

[14]DeLoach, R., "Applications of Modern Experiment Design to Wind Tunnel Testing at NASA Langley Research Center," AIAA Paper 98-0713, Jan. 1998.

[15]Giunta, A. A., Balabanov, V., Haim, D., Grossman, B., Mason, W. H., Watson, L. T., and Haftka, R. T., "Multidisciplinary Optimisation of a Supersonic Transport Using Design of Experiments Theory and Response Surface Modelling," *The Aeronautical Journal*, Vol. 101, No. 1008, 1997, pp. 347–356.

[16]Knill, D. L., Giunta, A. A., Baker, C. A., Grossman, B., Mason, W. H., Haftka, R. T., and Watson, L. T., "HCST Configuration Design Using Response Surface Approximations of Supersonic Euler Aerodynamics," AIAA Paper 98-0905, Jan. 1998.

[17]Tolle, R., "A New Optimum Design Code for Hypersonic Nozzles, Utilizing Response Surface Methodology," AIAA Paper 97-0519, Jan. 1997.

[18]Smith, T. D., Steffen, C. J., Jr., Yungster, S., and Keller, D. J., "Performance of an Axi-Symmetric Rocket-Based Combined-Cycle Engine During Rocket Only Operation Using Linear Regression Analysis," NASA TM 206632, March 1998.

[19]Spalart, P. R., and Allmaras, S. R., "A One-Equation Turbulence Model for Aerodynamic Flows," Le Recherche Aérospatiale, No. 1, 1994, pp. 5–22.

[20]Chien, K.-Y., "Predictions of Channel and Boundary Layer Flows with a Low-Reynolds-Number Turbulence Model," *AIAA Journal*, Vol. 20, No. 1, 1982, pp. 33–38.

[21]Sarkar, S., Erlebacher, G., Hussaini, M. Y., and Kreiss, H. O., "The Analysis and Modeling of Dilatation Terms in Compressible Turbulence," *Journal of Fluid Mechanics*, Vol. 227, 1991, pp. 473–493.

[22]Gordon, S., and McBride, B. J., "Computer Program for Calculation of Complex Chemical Equilibrium Compositions, Rocket Performance, Incident and Reflected Shocks, and Chapman-Jouguet Detonations," NASA SP-273, 1971.

[23]Pointwise, Inc., *Gridgen User's Manual, Version 11*, Bedford, TX, 1996.

[24]Mitchell, T. J., "An Algorithm for the Construction of 'D-Optimal' Experimental Designs," *Technometrics*, Vol. 16, No. 2, 1974, pp. 203–210.

[25]Bolt Beranek and Newman, Inc., *RS/1 Statistical Tools, User's Guide*, Cambridge, MA, 1990.

[26]Roache, P. J., "Perspective: A Method for Uniform Reporting of Grid Refinement Studies," *Journal of Fluids Engineering*, Vol. 116, No. 3, 1994, pp. 405–413.

[27]Quirk, J. J., "A Contribution to the Great Riemann Solver Debate," *International Journal for Numerical Methods in Fluids*, Vol. 18, No. 6, 1994, pp. 555–574.

[28]Rao, G. V. R., "Exhaust Nozzle Contour for Optimum Thrust," *Jet Propulsion*, Vol. 28, No. 6, 1958, pp. 377–382.

[29]Anderson, J. D., Jr., *Hypersonic and High Temperature Gas Dynamics*, McGraw–Hill Series in Aeronautical and Aerospace Engineering, New York, 1989, pp. 321–332.